

To appear in *Vehicle System Dynamics*
 Vol. 00, No. 00, Month 20XX, 1–20

Handling performance of a vehicle with different front-to-rear wheel torque distribution

B. Lenzo^{a*}, F. Bucchi^b, A. Sorniotti^c, and F. Frendo^b

^a*Department of Engineering and Mathematics, Sheffield Hallam University, Sheffield, UK;*

^b*Dipartimento di Ingegneria Civile e Industriale, Università di Pisa, Pisa, Italy;*

^c*Centre for Automotive Engineering, University of Surrey, Guildford, UK*

(WORD COUNT 6400)

The handling characteristic is a classical topic of vehicle dynamics. Usually, the handling is studied through the analysis of the understeer coefficient in quasi-steady state maneuvers, without considering the influence of the vehicle speed and the front-to-rear wheel torque distribution. In this paper, experimental maneuvers performed on a vehicle equipped with four independent motors, able to produce Front-Wheel-Drive, Rear-Wheel-Drive and All-Wheel-Drive (FWD, RWD and AWD respectively) architectures, are considered to infer the handling characteristics of each architecture through classical and new concepts. A procedure aimed at computing the longitudinal and lateral tire forces at each wheel is presented, which is based on a first estimate and a subsequent correction of the tire forces able to guarantee the vehicle equilibrium. The yaw moment analysis is then performed starting from the computed tire forces, aimed at identifying the contribution of the longitudinal and lateral forces to the vehicle yaw characteristics. The results show a fairly good agreement between the classical and the new formulation of the understeer coefficient and allow to infer a relationship between the understeer coefficient and the yaw moment analysis. The handling characteristics obtained for the considered maneuvers result different depending on vehicle speed and front-to-rear wheel torque distribution. In particular, an apparently surprising result arises at low speed, being the RWD architecture the most understeering. This result is discussed through the yaw moment analysis, highlighting the yawing effect of the longitudinal forces of the front tires, remarkable for high values of lateral acceleration and steering angle.

Keywords: Electric vehicles, yaw moment, handling, understeer, experiments, steering pad, FWD, RWD

1. Introduction

The handling characteristics of a vehicle are key factors for safety and performance. Vehicle models for the investigation of the vehicle cornering response have been developed since 1960s [1, 2]. The concepts of handling diagram and understeer coefficient were first introduced in [3], based on linearized single-track vehicle models for steady-state cornering conditions. Further studies lead to the characterization of the transient vehicle response, first using the single-track model, and then with the progressive introduction of more advanced simulators, allowing for instance to include non-linear tire force characteristics and suspension elasto-kinematics [4–8].

In more recent years, there has been a change of focus from the sole characterization

*Corresponding author. Email: basilio.lenzo@shu.ac.uk

of vehicle cornering response to its alteration, and even complete redesign according to desired criteria. This can be achieved using direct yaw moment control (DYC), i.e., the possibility to generate a yaw moment due to different longitudinal tire forces usually between the left and right hand sides of the vehicle. In first instance, DYC was attained with the individual control of the friction brakes at each wheel, to achieve stability control in extreme transient conditions, e.g. during emergency maneuvers [9, 10]. More recently, the advent of electric vehicles led to new vehicle architecture concepts, such as vehicles with multiple motors (e.g. one per axle, one per wheel etc. [11]), allowing torque-vectoring i.e. the ability to allocate desired wheel torque demands to each electric motor. Several authors (for example, [12–15]) proposed continuously active DYC controllers, with the specific purpose of designing the vehicle handling characteristic according to multiple driving modes selectable by the user. Such torque-vectoring based DYC algorithms were experimentally assessed on electric vehicles with multiple motors. Generally, these advanced controllers require the design engineer to define a reference value of vehicle yaw rate, based on the desired level of understeer or oversteer [16], geometrical parameters of the vehicle, tire-road friction conditions [17], and measurable vehicle states such as the steering wheel angle [18]. The reference yaw rate is compared online to the actual yaw rate measured on the vehicle, providing the basis for the calculation of the direct yaw moment [19]. In some instances the control strategy is also function of the vehicle sideslip angle [14], which can be either measured or estimated [20].

As discussed in [21, 22], the longitudinal tire forces affect the cornering response also in more conventional vehicle layouts, i.e. without torque-vectoring capabilities, depending on the differential typology and operating conditions. Considering an architecture with open differential, [23] presents a detailed yaw moment analysis on the level of vehicle understeer and oversteer, assessing the influence of the individual yaw moment contributions on different architectures implemented on the same vehicle plant. The analysis of the yaw moment effects related to the lateral tire forces and longitudinal tire forces shows differences in the cornering responses of Front-Wheel-Drive, Rear-Wheel-Drive and All-Wheel-Drive architectures (indicated as FWD, RWD and AWD in the remainder). In a steering pad maneuver, the RWD vehicle resulted more understeering than the FWD and AWD configurations, which is contrary to common belief [24]. The reduced level of understeer of the FWD configuration is caused by the destabilizing yaw moment of the lateral component (in the vehicle reference system) of the front longitudinal tire forces in traction. Another recent work [25] studies the impact of different architectures on the steady-state handling diagram at the limits of handling, presenting a case study for a generic oversteer vehicle. In [26], a simple strategy is introduced to enhance the maneuverability of a vehicle and reduce the cornering resistance with the appropriate allocation of wheel torques, for FWD, RWD and AWD layouts. As of yet, these findings present only simulation results. The only preliminary experimental assessment appears to be the authors' previous work [27]. Finally, [23] proposes a new definition of understeering coefficient in quasi-steady state maneuvers, yet again there does not exist an experimental validation of its accuracy in the literature.

This paper aims to fill this literature gap with the following contributions:

- the experimental validation of the new definition of understeering coefficient;
- the development of a vehicle model able to justify the experimental results, including a detailed analysis of the individual yaw moment contributions;
- the experimental analysis of the influence of the yaw moment on the cornering behaviour, with particular emphasis on the effects of the FWD, RWD and AWD layouts, which are presented and discussed with reference to the experimentally measured han-

Table 1.: Main vehicle parameters.

Symbol	Name and unit	Value
m	Mass (kg)	2290
J	Moment of inertia, vertical axis (kg m ²)	2761
a_1	Front semi-wheelbase (m)	1.365
l	Wheelbase (m)	2.665
τ	Transmission ratio (-)	10.56
R_w	Wheel radius (m)	0.364
w	Track width (m)	1.616
A_f	Frontal area (m ²)	2.69
C_x	Drag coefficient (-)	0.389
k_ϕ	Total roll stiffness (Nm/rad)	190000
$k_{\phi 1}$	Front axle roll stiffness (Nm/rad)	102600
$k_{\phi 2}$	Rear axle roll stiffness (Nm/rad)	87400
h	Center of gravity height (m)	0.55
d_1	Front roll center height (m)	0.15
d_2	Rear roll center height (m)	0.15

dling diagrams.

Section 2 presents the experimental tests, describing the equipment used, the maneuvers performed, and the adopted signal processing techniques. Section 3 focuses on the vehicle model and the numerical methods developed to estimate the tire-road forces, combining a mathematical model of vehicle and tires with relevant data measured by sensors. Results of the theoretical studies and experimental tests are analyzed and discussed in Section 4. Conclusions are summarized in Section 5.

2. Experimental tests

Several ramp steer maneuvers were performed with a fully electric vehicle demonstrator with four on-board motors, allowing the controlled implementation of any front-to-rear or left-to-right wheel torque distribution.

2.1. Test equipment and procedure

The experimental study was conducted at the Lommel proving ground (Belgium), on the electric Range Rover Evoque prototype (Figure 1) of the European Union funded project iCOMPOSE. The vehicle demonstrator features four identical on-board drivetrains, each of them consisting of a switched reluctance electric motor, a double-stage single-speed transmission system, constant velocity joints and a half-shaft. The main geometric and inertial parameters of the vehicle are reported in Table 1.

The test vehicle included the following sensors: i) a steering wheel angle sensor, measuring the steering wheel input applied by the driver, δ_w ; ii) a Corrsys Datron S – 350 sensor, installed on the front end of the car (see Figure 1), providing vehicle sideslip angle, β_{DAT} , and vehicle speed, V ; iii) an Inertial Measurement Unit (IMU), measuring longitudinal acceleration, a_x , lateral acceleration, a_y , and yaw rate, r ; iv) wheel speed sensors, providing the angular speed of each wheel, i.e., ω_{ij} , with $i = 1, 2$ (front, rear) and $j = 1, 2$ (left, right); and v) battery current and voltage sensors.

The tests consisted of ramp steer maneuvers executed at different reference speeds, i.e. 30 km/h, 60 km/h and 80 km/h. The desired vehicle speed was maintained throughout the maneuvers by means of a PI (Proportional Integral) speed tracking feedback controller, which provided the overall motor torque demand, T_T , based on the comparison



Figure 1.: The iCOMPOSE electric vehicle demonstrator with the Corrsys Datron sensor installed on the front end (Lommel proving ground, Belgium).

between reference speed and actual speed. The individual torque demands T_{11} , T_{12} , T_{21} , T_{22} , were then calculated from T_T depending on the desired layout (FWD, RWD, AWD with 50 – 50 front-rear distribution) using a dSPACE Autobox. In all cases wheel torques were evenly distributed among the left- and right-hand sides.

The test protocol was the following:

- (1) the vehicle was accelerated from standstill to the reference speed in a straight line, using the PI speed tracking controller;
- (2) once the reference speed was reached, a steering wheel angle ramp was applied by the driver with approximately constant rate. A small value of steering wheel rate was selected, ≈ 2 deg/s, to make the vehicle operate close to its steady-state condition;
- (3) the test was considered completed when the vehicle yaw rate reached its saturation level, i.e., when the yaw acceleration dropped to zero;
- (4) steps (1)-(3) were repeated for the three vehicle speeds (30 km/h, 60 km/h and 80 km/h), and three wheel torque distributions (FWD, RWD, AWD 50-50).

2.2. Signal processing and filtering

The relevant vehicle dynamics variables were obtained combining measurements and geometrical parameters, using the adapted ISO sign convention [28] (adopted throughout the paper).

The value of sideslip angle at the center of mass of the vehicle, β (this location is the most commonly used in the literature, [14]), was obtained combining β_{DAT} with the yaw rate r and with the longitudinal component of the vehicle center of mass velocity, u [29, 30]:

$$\tan \beta = \tan \beta_{DAT} - \frac{r}{u}(d + a_1) \quad (1)$$

where d is the longitudinal distance between the front axle of the vehicle and the Datron sensor.

The steering ratio of the car can be considered constant only in first approximation, for limited values of the steering wheel angle. Owing to the high values of steering angles intrinsic of these experiments, an experimental non-linear map was created, providing the steering angles of the left and right wheels, δ_{11} and δ_{12} , as functions of δ_w (Figure

2).

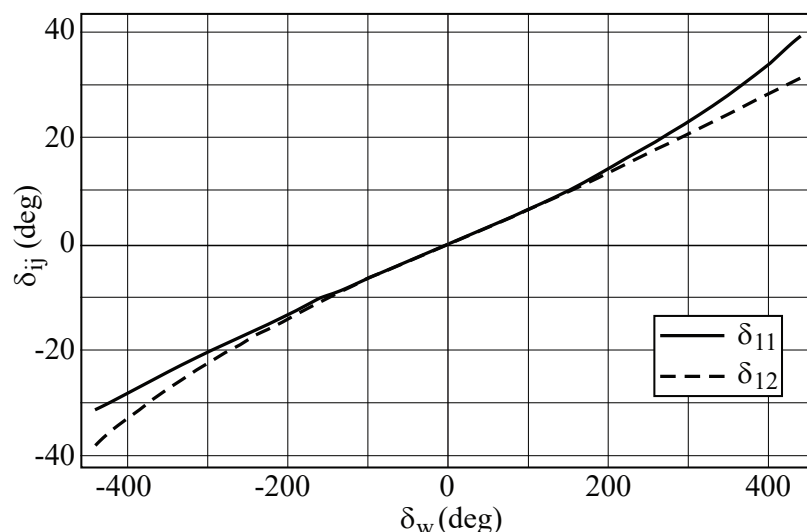


Figure 2.: Steering angle of front left and front right wheel vs. steering wheel angle.

Appropriate filtering techniques were adopted to attenuate the effect of measurement noise. The input of the filtering process was the relevant part of each recorded signal, i.e. from when the driver starts to apply a steering input to when the yaw rate saturates, as described in the test protocol. This was justified by the presence of swift changes of the signals just outside their relevant part (e.g. see Figure 4).

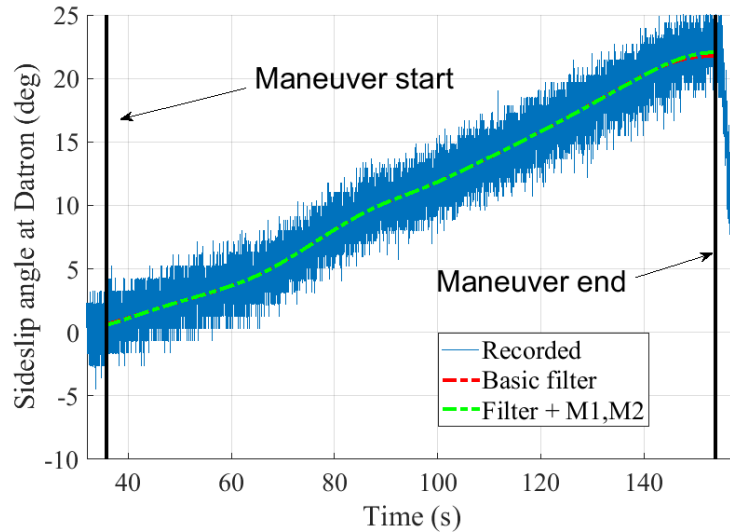
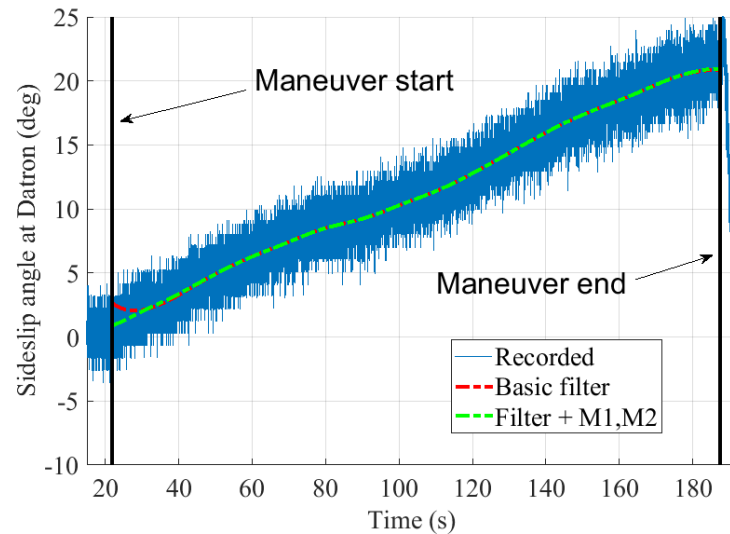
The Matlab "filtfilt" function was used. Its main benefit is the execution of a forward-backward filtering, averting phase lags. Notwithstanding, "filtfilt" might introduce undesired boundary effects at the beginning and/or end of the filtered signal. Such boundary effects have been addressed using the following Methods:

M1 where needed, introducing a predetermined amount of reflected copies of the signal, either at the beginning or at the end of the relevant part of the signal;

M2 where needed, extending the timeframe beyond the relevant part of the recorded signal by a predetermined amount of time, at the beginning and/or at the end of the relevant part of the signal.

Based on the time history and on the effect of each Method, a careful analysis was performed for each measured signal. As a result, either Method 1 (M1), Method 2 (M2), or a combination of them, were adopted, with appropriate tuning parameters (length of the reflected copies for M1, amount of extra time for M2).

Figures 3 and 4 show examples of filtered functions, using "filtfilt" only (basic filter) and using "filtfilt" in addition with the above methods. The black vertical bars represent the boundaries of the relevant part of the signal, as defined earlier. Figure 3 shows the effect of a partial reflection of the signal (M1) at the end of a maneuver, due to the signal suddenly dropping at the end of the maneuver. On the other hand, in Figure 4, the extension of the timeframe (M2) slightly before the start of the maneuver results beneficial.

Figure 3.: Signal filtering: β_{DAT} , maneuver 30 km/h AWD.Figure 4.: Signal filtering: β_{DAT} , maneuver 30 km/h RWD.

3. Numerical models for tire forces computation

In order to consider the influence of the wheel torque distribution on the vehicle dynamics, the longitudinal and lateral forces acting at each tire to ground interface should be known, since, as discussed in [23], these affect the yaw moment contributions. However, the acquired signals do not directly provide the longitudinal and lateral forces, so a vehicle and tire model was needed to compute them starting from the acquired signals.

The simple vehicle model described in Section 3.1 was developed and implemented to obtain a first general estimate of the tire forces. In particular, the longitudinal forces were estimated considering each motor torque demand ($T_{11}, T_{12}, T_{21}, T_{22}$) at each time-step. The lateral forces were estimated with a pure-lateral Pacejka tire model, based on the

tire slip angle and the vertical force of each tire at each time step. Tire slip angles were computed with classical in-plane kinematics [30], vertical forces were calculated considering the vehicle mass distribution along with longitudinal and lateral load transfers, based on the measured accelerations.

Subsequently, the vehicle equilibrium was considered and the estimated longitudinal and lateral tire forces were corrected in order to match the measured longitudinal, lateral and yaw accelerations at each time step, as described in Section 3.2.

3.1. Tire forces estimation

A double-track model was developed to assess the longitudinal and lateral forces starting from the data acquired on the real vehicle. The model, shown in Figure 5, considers a rigid body having mass m and yaw moment of inertia J , moving on a flat surface. The forces acting on the rigid body are the longitudinal X_{ij} and lateral Y_{ij} forces of each tire (as shown in Section 2, $i = 1, 2$ for front and rear, $j = 1, 2$ for left and right), and the drag force F_D due to aerodynamic and rolling resistance, which is assumed to be applied in the center of gravity G . The self aligning moment are neglected in this model. The front left and front right wheels can steer (angles δ_{11} and δ_{12} respectively), while the rear wheels cannot. The vehicle geometry is described through the front and rear semi-wheelbases a_1 and a_2 respectively, the wheelbase l , the front track t_1 and the rear track t_2 . The geometrical parameters are assumed constant during the vehicle motion.

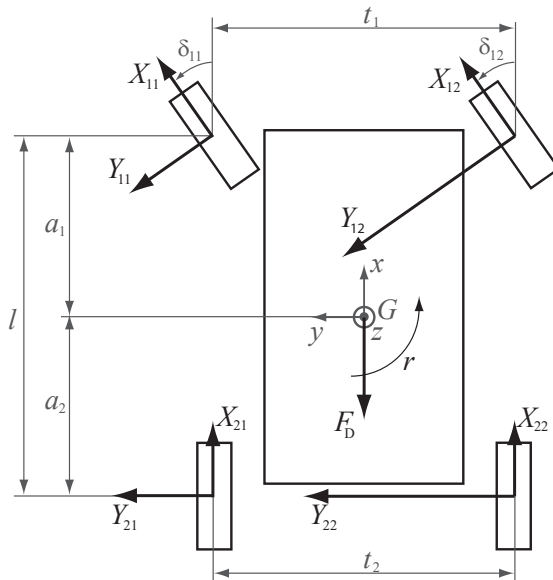


Figure 5.: Double-track vehicle model.

The longitudinal forces X_{ij} of the driving wheels were assessed based on each motor torque T_{ij} , neglecting inertial effects:

$$X_{ij} = \frac{\eta\tau T_{ij}}{R_w} \quad (2)$$

where τ is the motor-to-wheel transmission gear ratio and η the motor and transmission

efficiency. The longitudinal force of the non-driven wheels were assumed equal to 0. The lateral forces Y_{ij} were assessed considering the lateral tire slip angles α_{ij} , the vertical force at each tire Z_{ij} and the lateral force (pure side-slip) defined by the constitutive model PAC2002 [28], neglecting camber angle and other secondary effects, as follows:

$$Y_{ij} = D \sin(C \arctan(B(\alpha_{ij} + S_{Hy}) - E(B(\alpha_{ij} + S_{Hy}) - \arctan B(\alpha_{ij} + S_{Hy})))) + S_{V_y} \quad (3)$$

where B , C are tire parameters, D and E are tire parameters related to the tire vertical force Z_{ij} , e.g. $D = \mu Z_{ij} \zeta_2$, where μ is the adherence and ζ_2 is a correction parameter, while S_{Hy} and S_{V_y} are curve translational parameters. The lateral tire slip angles α_{ij} are given by

$$\alpha_{ij} = \delta_{ij}^0 + \delta_{ij}(\delta_w) - \beta + (-1)^i a_i \frac{r}{u} \quad i = 1, 2; \quad j = 1, 2 \quad (4)$$

where δ_{ij}^0 is the static toe of each wheel, experimentally measured, and the law $\delta_{ij}(\delta_w)$ is known for the tested vehicle (Figure 2).

The vertical forces Z_{ij} were assessed under the steady-state hypothesis, starting from the longitudinal and lateral accelerations and the front and rear roll stiffness, k_ϕ^1 and k_ϕ^2 respectively:

$$Z_{ij} = \frac{mg(l - a_i)}{2l} + (-1)^i \frac{mh}{2l} a_x + (-1)^j \frac{m a_y}{t_i} \left(\frac{(l - a_i)d_i}{l} + \frac{k_\phi^i}{k_\phi^1 + k_\phi^2} (h - d) \right) \quad i = 1, 2; \quad j = 1, 2 \quad (5)$$

where g is the gravity acceleration, a_x and a_y are the longitudinal and lateral acceleration of the vehicle center of gravity, h the center of gravity height, d_i the i -th roll center height, d the height of the intersection point between the roll axis and a y-z plane passing through the center of gravity.

Both the longitudinal and lateral acceleration models are intentionally simple, because no information about the suspension geometry, the actual tire to ground adherence and the temperature effect on the tire force need to be assumed to implement this model, which will be correct by the algorithm described in the following section.

3.2. Tire forces correction

Considering the vehicle model shown in Figure 5, the longitudinal, lateral and yaw equilibrium of the vehicle is expressed by

$$ma_x = X_{11} \cos \delta_{11} + X_{12} \cos \delta_{12} + X_{21} + X_{22} - Y_{11} \sin \delta_{11} - Y_{12} \sin \delta_{12} - F_D \quad (6a)$$

$$ma_y = Y_{11} \cos \delta_{11} + Y_{12} \cos \delta_{12} + Y_{21} + Y_{22} + X_{11} \sin \delta_{11} + X_{12} \sin \delta_{12} \quad (6b)$$

$$\begin{aligned} J\dot{r} = & (Y_{11} \cos \delta_{11} + Y_{12} \cos \delta_{12} + X_{11} \sin \delta_{11} + X_{12} \sin \delta_{12})a_1 - (Y_{21} + Y_{22})a_2 + \\ & + (X_{12} \cos \delta_{12} - X_{11} \cos \delta_{11})t_1/2 + (X_{22} - X_{21})\frac{t_2}{2} + (Y_{11} \sin \delta_{11} - Y_{12} \sin \delta_{12})t_1/2 \end{aligned} \quad (6c)$$

As discussed in Section 2.1, the longitudinal and lateral accelerations of the vehicle center of mass (a_x and a_y respectively), are measured by on-board accelerometers. The

yaw acceleration \dot{r} can be derived by the yaw rate r measured by the gyroscope. Again, the steering angle of the front left and front right wheel can be computed considering the measured steering wheel angle δ_w and the steering law shown in Figure 2. The drag force F_D is computed at each step as:

$$F_D = \frac{1}{2} \gamma C_x A u^2 + F_R \quad (7)$$

where γ is the air density, C_x the longitudinal drag coefficient, A the vehicle frontal area, u the longitudinal component of the vehicle center of mass velocity, and F_R the overall rolling resistance force, assumed constant.

The equilibrium equation given in Eq. 6 can be written in the compact form $A\mathbf{x} = \mathbf{b}$, where the parameter matrix A is (cosine and sine functions are abbreviated respectively as c and s)

$$A = \begin{bmatrix} c_{\delta_{11}} & c_{\delta_{12}} & 1 & 1 & -s_{\delta_{11}} & -s_{\delta_{12}} & 0 & 0 \\ s_{\delta_{11}} & s_{\delta_{12}} & 0 & 0 & c_{\delta_{11}} & c_{\delta_{12}} & 1 & 1 \\ a_1 s_{\delta_{11}} - \frac{t_1}{2} c_{\delta_{11}} & a_1 s_{\delta_{12}} + \frac{t_1}{2} c_{\delta_{12}} & -\frac{t_2}{2} & \frac{t_2}{2} & a_1 c_{\delta_{11}} + \frac{t_1}{2} s_{\delta_{11}} & a_1 c_{\delta_{12}} - \frac{t_1}{2} s_{\delta_{12}} & -a_2 & -a_2 \end{bmatrix} \quad (8)$$

the estimated tire force vector \mathbf{x} is

$$\mathbf{x} = [X_{11} \ X_{12} \ X_{21} \ X_{22} \ Y_{11} \ Y_{12} \ Y_{21} \ Y_{22}]^T \quad (9)$$

and the inertial and drag force vector \mathbf{b} is

$$\mathbf{b} = [ma_x + F_D \ ma_y \ J\dot{r}]^T \quad (10)$$

It is worth noting that, at each time-step: i) the parameters included in A are known based on the vehicle geometry, measured steering wheel angle and steering law; ii) the forces included in \mathbf{b} are known based on the measured accelerations, yaw rate and on the drag force equation (Eq. 7); iii) the tire forces \mathbf{x} are estimated as described in Section 3.1.

Due to the simplifying hypotheses introduced in the numerical model and to the differences between the pure-lateral part of the PAC2002 tire model and the actual tire on the car, the left and right terms of the equilibrium equations Eq. 6 are not equal in general. For this reason, a vector $\Delta\mathbf{x}$ is introduced to correct the estimated tire forces \mathbf{x} , such that the equilibrium is actually satisfied:

$$A(\mathbf{x} + \Delta\mathbf{x}) = \mathbf{b} \quad (11)$$

Being A not a square matrix, its pseudoinverse $A^+ = A^T(AA^T)^{-1}$ is required to calculate $\Delta\mathbf{x}$:

$$\Delta\mathbf{x} = A^+(\mathbf{b} - A\mathbf{x}). \quad (12)$$

Owing to the pseudoinverse properties [31], $\Delta\mathbf{x}$ is the minimum norm vector that, added to \mathbf{x} , allows the equilibrium equations to be satisfied. Equation 12 contemplates all the components of $\Delta\mathbf{x}$ in the same way, without considering that they may have different orders of magnitude (e.g. if the lateral acceleration is high, due to lateral load

transfer, the lateral force at inner tires are much lower than the lateral force at outer tires). To obtain a more realistic estimation, a weight matrix W was introduced:

$$W = \begin{bmatrix} Z_{11}^{-1} & 0 & 0 & 0 & 0 & 0 & 0 & 0 \\ 0 & Z_{12}^{-1} & 0 & 0 & 0 & 0 & 0 & 0 \\ 0 & 0 & Z_{21}^{-1} & 0 & 0 & 0 & 0 & 0 \\ 0 & 0 & 0 & Z_{22}^{-1} & 0 & 0 & 0 & 0 \\ 0 & 0 & 0 & 0 & Z_{11}^{-1} & 0 & 0 & 0 \\ 0 & 0 & 0 & 0 & 0 & Z_{12}^{-1} & 0 & 0 \\ 0 & 0 & 0 & 0 & 0 & 0 & Z_{21}^{-1} & 0 \\ 0 & 0 & 0 & 0 & 0 & 0 & 0 & Z_{22}^{-1} \end{bmatrix} \quad (13)$$

Each diagonal element kk of W is the reciprocal of the vertical load acting on the tire considered in the k -th element of \mathbf{x} (e.g. $W_{33} = Z_{21}^{-1}$ because $\mathbf{x}_3 = X_{21}$, see Eq. 9).

This allows to normalize the contribution of each element of $\Delta\tilde{\mathbf{x}}$, i.e. each correction term (k -th element of $\Delta\tilde{\mathbf{x}}$, see Eq. 9) is proportional to the actual vertical load Z_{ij} on that tire.

In addition, two rows were added to the matrix A and to the vector \mathbf{b} to guarantee $X_{11} = X_{12}$ and $X_{21} = X_{22}$, which follows from the wheel torque allocation (see Section 2.1). The matrix A_1 and the vector \mathbf{b}_1 were then defined as

$$A_1 = \begin{bmatrix} c_{\delta_{11}} & c_{\delta_{12}} & 1 & 1 & -s_{\delta_{11}} & -s_{\delta_{12}} & 0 & 0 \\ s_{\delta_{11}} & s_{\delta_{12}} & 0 & 0 & c_{\delta_{11}} & c_{\delta_{12}} & 1 & 1 \\ a_1 s_{\delta_{11}} - \frac{t_1}{2} c_{\delta_{11}} & a_1 s_{\delta_{12}} + \frac{t_1}{2} c_{\delta_{12}} & -\frac{t_2}{2} & \frac{t_2}{2} & a_1 c_{\delta_{11}} + \frac{t_1}{2} s_{\delta_{11}} & a_1 c_{\delta_{12}} - \frac{t_1}{2} s_{\delta_{12}} & -a_2 & -a_2 \\ 1 & -1 & 0 & 0 & 0 & 0 & 0 & 0 \\ 0 & 0 & 1 & -1 & 0 & 0 & 0 & 0 \end{bmatrix} \quad (14)$$

$$\mathbf{b}_1 = [ma_x + F_D \ ma_y \ J\dot{r} \ 0 \ 0]^T \quad (15)$$

The definition of A_1 and \mathbf{b}_1 are valid for the AWD architecture, while only one additional row is necessary to guarantee $X_{11} = X_{12}$ for the FWD layout and $X_{21} = X_{22}$ for the RWD layout. It is worth noting that the assumption of equal forces on the same axle is valid if the adherence limit is not overcome by any tire, otherwise dynamic equations for each wheel dynamics should be considered.

The weight matrix was then introduced in the pseudoinverse definition [32]:

$$\tilde{A}_1^+ = W^{-1} A_1^T (A_1 W^{-1} A_1^T)^{-1} \quad (16)$$

and the tire force correction vector $\Delta\tilde{\mathbf{x}}$ was consequently computed as

$$\Delta\tilde{\mathbf{x}} = \tilde{A}_1^+ (\mathbf{b}_1 - A_1 \mathbf{x}). \quad (17)$$

Finally, the corrected tire forces $\tilde{\mathbf{x}}$ were obtained as follows

$$\tilde{\mathbf{x}} = \mathbf{x} + \Delta\tilde{\mathbf{x}}. \quad (18)$$

4. Results and discussion

In this section the results obtained directly from the tests and indirectly through the tire force estimation are shown. Firstly, the understeer characteristics obtained for each maneuver are shown, using both the classical and an alternative definition of the understeer coefficient. Then, the estimated forces are firstly estimated and then corrected, basing on the procedure described in Section 3. These force results are used to infer the yaw moment analysis and the different yaw components contributing to the are analyzed, introducing also the relationship between the understeer coefficient and the yaw moment analysis.

4.1. Understeer coefficients and handling diagram

In order to compare the handling of the vehicle for different speeds and drivetrain architectures, the understeer coefficient K was considered, using both the classical definition [3] and the definition proposed in [23], denoted as "new definition" in the remainder. In particular, the classical definition is:

$$K = \frac{\partial(\alpha_1 - \alpha_2)}{\partial \tilde{a}_y} \quad (19)$$

where α_1 and α_2 are the front and rear slip angle in the single-track model and $\tilde{a}_y = u^2 \rho$ is the steady-state lateral acceleration, where $\rho = 1/r$. Considering the congruence equations of the single-track model, the understeer coefficient is

$$K = \frac{\partial(\bar{\delta} - l\rho)}{\partial \tilde{a}_y} = \frac{\partial \delta_{\text{dyn}}}{\partial \tilde{a}_y} \quad (20)$$

where $\bar{\delta}$ is the steering angle of the front wheel in the single-track model which can be generalized for the double track model as the average value of the steering angle of the front wheels, i.e. $\bar{\delta}(\delta_w) = \frac{\delta_{11}(\delta_w) + \delta_{12}(\delta_w)}{2}$.

As discussed in [23], the understeer coefficient can be computed considering a series of steady-state maneuvers at different lateral accelerations. Alternatively, the new definition of the understeer coefficient allows to obtain a fairly good estimation of K performing constant speed maneuvers with constant and small steering angle rate $\dot{\bar{\delta}}$ (as described in Section 2.1):

$$K \simeq \frac{1}{u^2} \left(\frac{\dot{\bar{\delta}}}{\dot{\rho}} - l \right). \quad (21)$$

Figure 6 reports the comparison of the understeer coefficient obtained considering the data acquired during the 60 km/h RWD maneuver, applying the classical and the new definitions. It is worth noting that, since the classical definition refers to steady-state condition, the data obtained during the ramp steer maneuvers could not be used. However, since the the maneuvers were performed in quasi steady-state conditions (i.e. steering wheel angle rate of about 2 deg/s), the understeer coefficient was computed considering $a_y(t)$ instead of \tilde{a}_y . The plot confirms that the two formulations are almost equivalent in the whole range of acceleration.

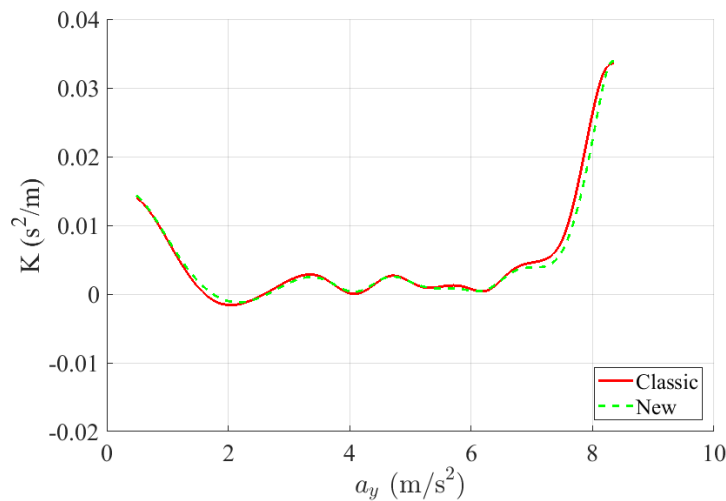


Figure 6.: Classic and new understeering coefficients for the 60 km/h RWD test.

Figure 7 reports the dynamic steering wheel angle as a function of lateral acceleration for the considered vehicle speeds. At a glance, the handling characteristics are grouped together on the basis of the vehicle speed. The maneuvers performed at 30 km/h show an oversteering behavior ($K < 0$) up to about 8 m/s^2 and then a strongly understeering behavior up to the maneuver interruption. Differently, the maneuvers performed at 60 km/h and 80 km/h show an understeering behavior of the vehicle in the whole acceleration range.

Comparing the maneuvers performed at the same speed, the resulting characteristics are very similar for the three powertrain architectures at 60 km/h and 80 km/h. A perceivable difference in the handling behavior of the three powertrain architectures is observed at 30 km/h and high a_y , with the RWD configuration being more understeering than the FWD and AWD ones.

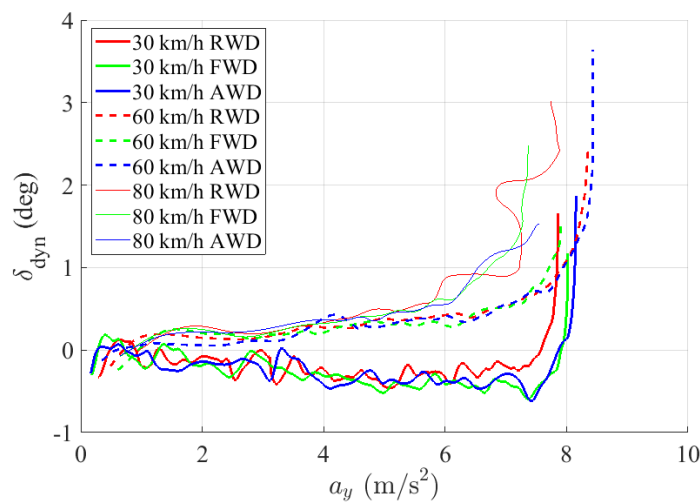


Figure 7.: Dynamic steering wheel angle as a function of the vehicle lateral acceleration.

4.2. Tire forces analysis

Following the procedure described in Section 3, the longitudinal and lateral forces at each tire were computed for each test. As an example of the results, considering the 60 km/h RWD test, Figure 8 shows the longitudinal forces firstly estimated as described in Section 3.1 and then corrected in order to satisfy vehicle equilibrium based on acquired data, as described in Section 3.2. Similarly, Figure 9 shows the estimated and corrected lateral forces for the same test. Concerning the longitudinal forces, the correction is small for the driven wheels while the non-driving wheels are not shown because they do not exert any appreciable force both in the estimated and in the corrected formulation. Regarding the lateral forces, the tire forces are generally lower than the corrected ones, especially at the rear tires and for low lateral acceleration values. The differences can be ascribed to the simplifying assumption made in the tire model considered for the estimation where the secondary effects are neglected, e.g. camber and temperature effects, and the adherence multiplying factor is assumed equal to 1, without information on the actual grip of the test road. Finally, the self-aligning moments were neglected in the vehicle equilibrium model (Eq. 6) and consequently this simplifying assumption affects the forces estimation. However, these assumptions are acceptable for a first raw forces estimation (Section 3.1), because the implemented correction guarantees vehicle equilibrium.

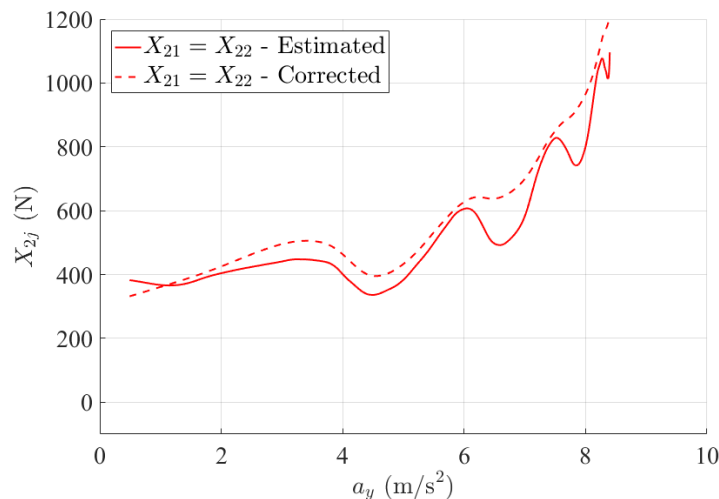


Figure 8.: Estimated and corrected longitudinal forces - 60 km/h RWD.

In order to verify that the corrected values of the forces did not overcome the adherence limit, the adherence index was computed as the ratio between the total force exerted by each tire (longitudinal and lateral) and the vertical force acting on the same tire

$$\mu_{ij} = \frac{\sqrt{X_{ij}^2 + Y_{ij}^2}}{Z_{ij}} \quad (22)$$

Figure 10 (right) shows the adherence index computed for all the tires during the test performed at 60 km/h with RWD layout. The maximum adherence is about 1.15 for internal tires and 0.8 for external ones. This difference is ascribable to the dependence of the adherence coefficient on the vertical load [30], which results lower for the tire loaded with higher vertical loads, i.e. external tires at high lateral acceleration. Figure 10 (left)

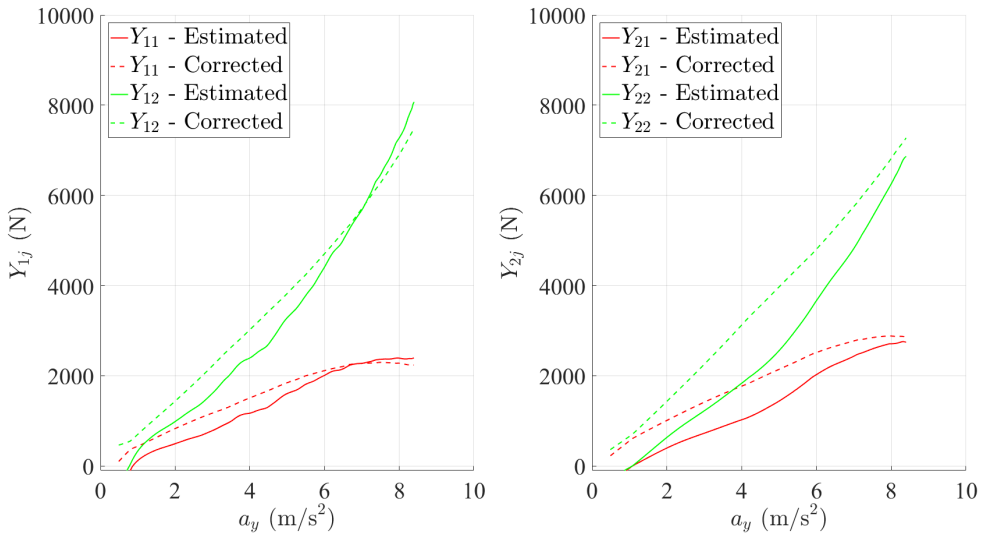


Figure 9.: Estimated and corrected lateral forces - 60 km/h RWD.

shows the adherence index computed for the same test without introducing the weight matrix W , which is substituted by an identity matrix. In this case the results are slightly different, especially for the internal tires, where the adherence of the internal front tire is underestimated, while the adherence on the internal rear tire is overestimated. As anticipated, the weight matrix W was introduced to reduce the correction on the low vertically loaded tires, guaranteeing that the correction on those tires weighs more in the computation of the least square norm correction vector $\Delta\tilde{x}$.

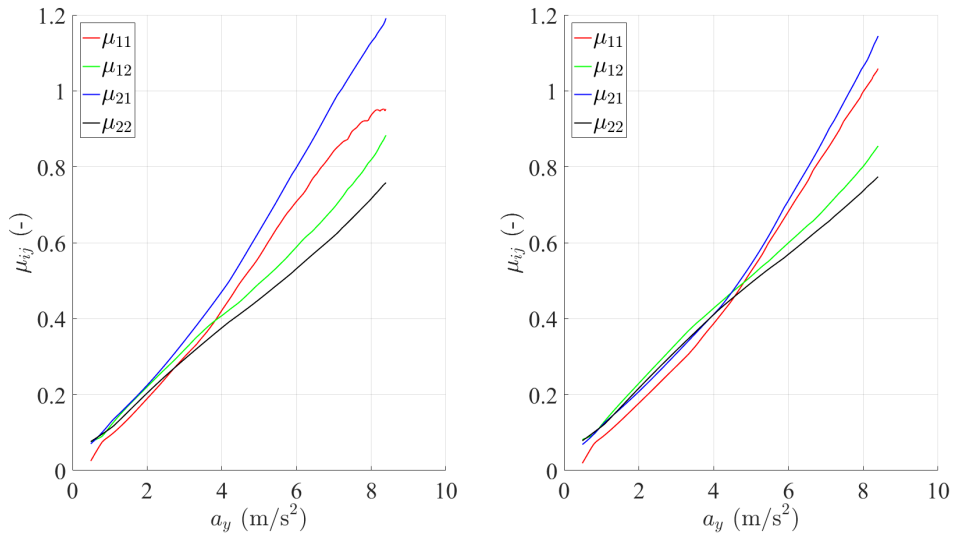


Figure 10.: Adherence index obtained correcting the forces without (left) using the weight matrix W and (right) using the weight matrix W - 60 km/h RWD.

4.3. Yaw moment analysis

In order to compute the yaw moment contribution of longitudinal and lateral forces, the total yaw moment N can be split in three terms, in accordance with the right-hand side of Eq. 6c, defined as follows

$$N_f = X_{11}a_1 \sin \delta_{11} + X_{12}a_1 \sin \delta_{12} \quad (23)$$

$$N_y = Y_{11}(a_1 \cos \delta_{11} + \frac{t_1}{2} \sin \delta_{11}) + Y_{12}(a_1 \cos \delta_{12} - \frac{t_1}{2} \sin \delta_{12}) - (Y_{21} + Y_{22})a_2 \quad (24)$$

$$N_d = (X_{12} \cos \delta_{12} - X_{11} \cos \delta_{11}) \frac{t_1}{2} + (X_{22} - X_{21}) \frac{t_2}{2} \quad (25)$$

such that $J\dot{r} = N = N_f + N_y + N_d$. The term N_f is the yaw moment contribution related to the longitudinal front tire forces, the term N_y is the yaw moment contribution of the lateral forces acting on all tires and the term N_d is the yaw moment contribution related to different components, along the longitudinal axis of the vehicle, of the drive forces of tires belonging to the same axle. Since we assumed $X_{11} = X_{12}$ and $X_{21} = X_{22}$, N_d is always nearly zero, except for high steering wheel angle values when δ_{11} and δ_{12} are considerably different and, consequently, the term $X_{12} \cos \delta_{12} - X_{11} \cos \delta_{11}$ is not zero even if $X_{11} = X_{12}$.

Figure 11 shows the yaw moment contributions for all the maneuvers. Concerning the maneuvers performed with the RWD architecture, the only contribution to the yaw moment is N_y , while $N_f = 0$ because no longitudinal force is exerted by the front tires, then $N = N_y$. As shown in Figure 11a, for the 30 km/h maneuver, N is almost constant in the whole lateral acceleration range, except at the end of the maneuver where N decreases steeply. Considering higher speed maneuvers, Figure 11b and Figure 11c, N is higher at the beginning of the maneuver and decreases as the lateral acceleration rises. Concerning the maneuvers performed with FWD and AWD architectures, the contribution of N_f is very significant; in particular N_f

- increases as the acceleration rises because, as discussed in [23] and [27], both the steering angles, δ_{11} and δ_{12} , and the longitudinal forces, X_{11} and X_{12} , rise;
- is greater for low speed maneuvers, where, for a given value of lateral acceleration, the steering angle is greater;
- is more pronounced in the maneuvers performed with FWD architecture because the total longitudinal force is exerted only by the front tires, then X_{11} and X_{12} are greater than for the AWD maneuver.

However, as the yaw contribution of the longitudinal forces rise, the yaw contribution due to the lateral force decreases. This phenomenon is related to the lower lateral force exerted by front tires with respect to the maneuvers performed with RWD architecture, due to the combined behavior of the tires.

Adding all the yaw moment contributions, the total yaw moment N is obtained for all the maneuvers, as shown in Figure 12. It is worth noting that, even if the single contributions are different, the total yaw moment is similar for all the drive architectures at a given speed. However, there are some differences for the 30 km/h maneuvers, i.e. N for FWD and AWD architectures is greater than for the RWD architecture in the

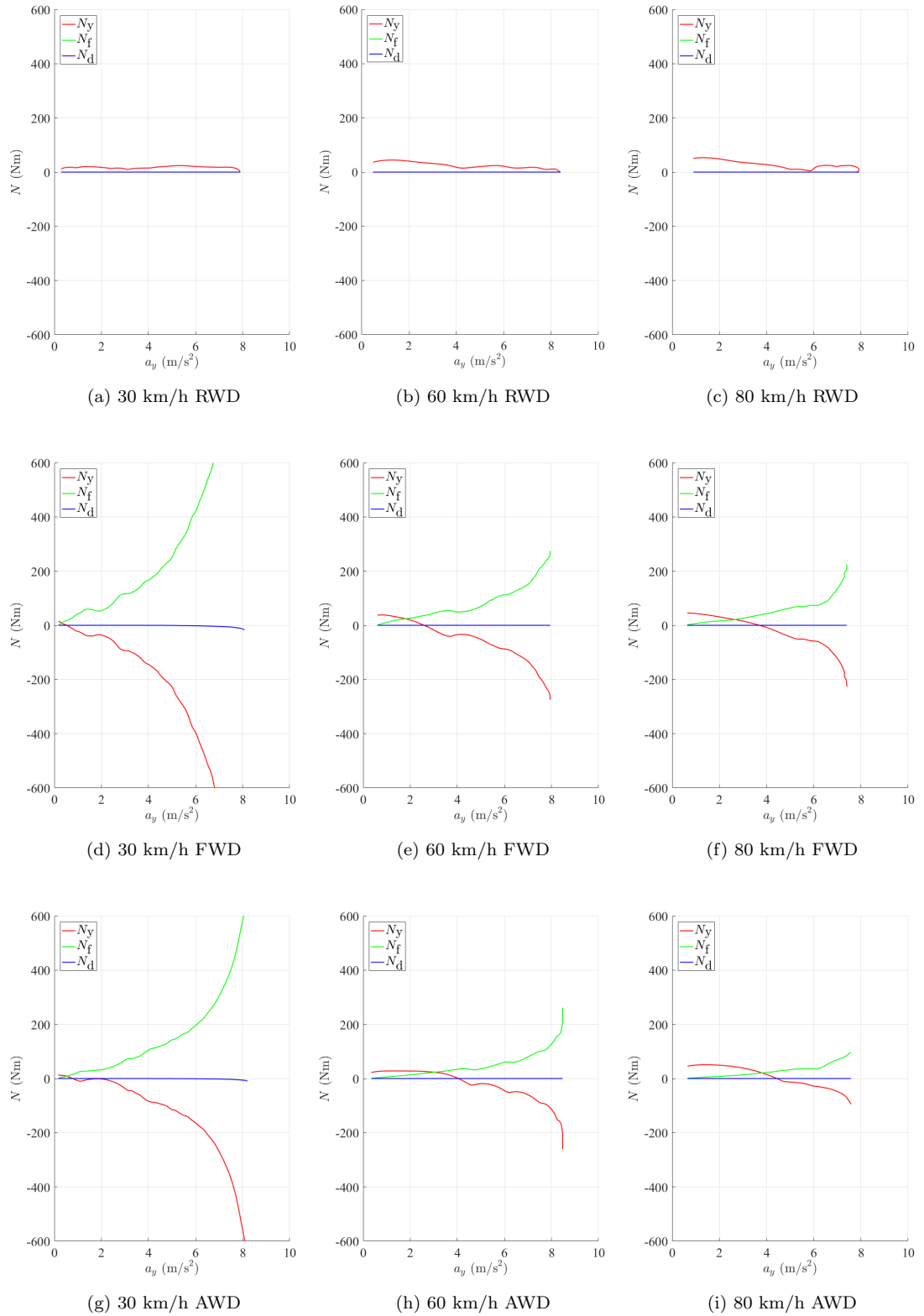


Figure 11.: Yaw moment contributions vs. lateral acceleration.

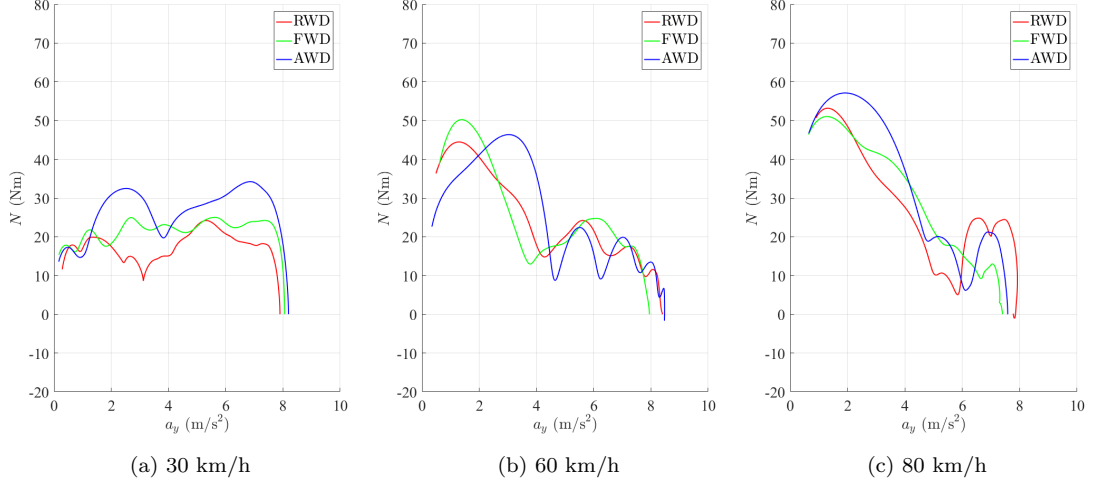


Figure 12.: Total yaw moment vs. lateral acceleration.

whole acceleration range. This is explained as, with increasing lateral acceleration, N_f rises more compared to the amount N_y lessens (see Figure 11).

In order to understand the relationship between the yaw moment plot and the understeer coefficient and, consequently, with the dynamic steering angle plot (Figure 7), it is useful to recall the definition of the understeer coefficient, as introduced in [23]

$$K = \frac{\partial \delta_{dyn}}{\partial a_y} \simeq \frac{1}{u^2} \left(\frac{\dot{\bar{\delta}}}{\dot{\rho}} - l \right) = \frac{1}{u^2} \left(\frac{\dot{\bar{\delta}} u J}{N} - l \right) = \frac{\dot{\bar{\delta}} J}{N u} - \frac{l}{u^2} \quad (26)$$

Given this relationship it is clear that, for a given maneuver ($\bar{\delta}$ and u), the greater is N the less understeering is the vehicle (lower K). Figure 13 shows the inverse of the yaw moment ($1/N$). Indeed Figure 13a, shows that the inverse of N computed for the 30 km/h maneuver performed with RWD architecture is always greater than the ones computed for FWD and AWD architectures, confirming the more understeering behavior of the vehicle set-up among the three considered drive-train architectures at 30 km/h. Considering higher speed maneuvers, no particular differences arise, as it was already clear in Figure 7. It is worth remarking that, from an on-board acquisition point of view, the computation of N can be easily made measuring the yaw rate derivative \dot{r} and multiplying it by J .

Finally, the relationship between the dynamic steering angle plot (Figure 7) and the total yaw moment is given by the following equation

$$\delta_{dyn} = \int_0^{\bar{a}_y} K da_y = \int_0^{\bar{a}_y} \frac{\dot{\bar{\delta}} J}{N u} da_y - \int_0^{\bar{a}_y} \frac{l}{u^2} da_y = \dot{\bar{\delta}} J \left(\frac{1}{u} \int_0^{\bar{a}_y} \frac{1}{N} da_y - \frac{l \bar{a}_y}{\dot{\bar{\delta}} J u^2} \right) \quad (27)$$

which is obtained by integration of Eq. 26, considering quasi steady-state conditions.

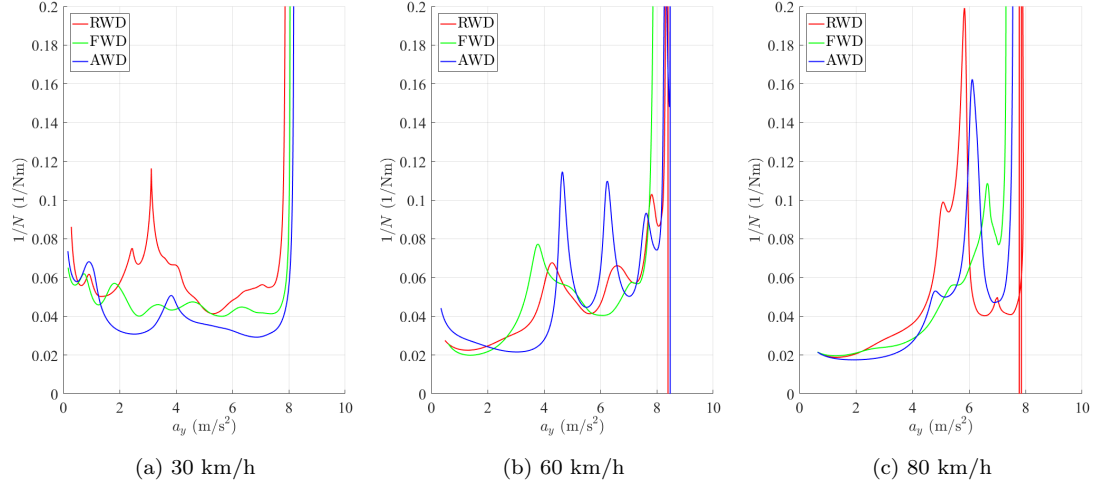


Figure 13.: Inverse of total yaw moment vs. lateral acceleration.

5. Conclusions

The analysis proposed in this paper allowed to compare the handling behavior of a vehicle equipped with four independent motors, one per wheel, controlled in order to obtain different drivetrain architectures. In particular, nine types of tests were conducted considering three different-speed steering ramp maneuvers, each one performed at constant speed with FWD, RWD and AWD drivetrain architectures.

The handling was analyzed in terms of understeer coefficient and dynamic steering angle plot, as usually done in the classical vehicle dynamics literature, considering also the new formulation of the understeer coefficient proposed in [23]. In addition, a procedure to estimate and correct the longitudinal and lateral tire forces was presented. Based on the motors torque demand, on a first estimate of the pure lateral force tire characteristic, and on the IMU acquired kinematic data, the procedure allowed to find the tire forces distribution able to satisfy vehicle equilibrium. Considering the obtained forces, the yaw moment analysis was performed, which allowed to isolate the contribution of the lateral and the longitudinal forces for the different maneuvers and powertrain architectures. In particular, for the 30 km/h maneuver, a surprising result arised as the RWD architecture resulted the most understeering. This can be ascribed, as already introduced in [27], to the destabilizing yaw moment produced by the longitudinal forces of the front tires, especially for high steering angle values. Such yaw moment affects the vehicle dynamics for FWD and AWD maneuvers, exceeding the lateral forces yaw moment loss due to the combined behavior of the front tires.

The results of this paper confirm the relationship between the classical handling analysis and the yaw moment analysis, which explains the effects of the longitudinal forces on the vehicle dynamics in quasi-steady state condition. Starting from the computation of the the yaw moment contribution, an optimal control of the driving forces could be implemented in the future.

6. Acknowledgement

The research leading to these results has received funding from the European Union Seventh Framework Programme FP7/2007-2013 under Grant Agreement No. 608897 (iCOMPOSE project).

References

- [1] Nordeen DL. Vehicle handling: Its dependence upon vehicle parameters. SAE Technical Paper; 1964. Report no.:.
- [2] Sheridan TB. Vehicle handling: Mathematical characteristics of the driver. SAE Technical Paper; 1963. Report no.:.
- [3] Pacejka HB. Simplified analysis of steady-state turning behaviour of motor vehicles. part 1. handling diagrams of simple systems. *Vehicle System Dynamics*. 1973;2(3):161–172.
- [4] Barter N. Analysis and interpretation of steady-state and transient vehicle response measurements. *Vehicle System Dynamics*. 1976;5(1-2):79–103.
- [5] VERMA MK. Transient response test procedures for measuring vehicle directional control. *Vehicle System Dynamics*. 1981;10(6):333–356.
- [6] Gim G. Vehicle dynamic simulation with a comprehensive model for pneumatic tires.. 1988;.
- [7] Farroni F, Russo M, Russo R, Terzo M, Timpone F. A combined use of phase plane and handling diagram method to study the influence of tyre and vehicle characteristics on stability. *Vehicle System Dynamics*. 2013;51(8):1265–1285.
- [8] Morales ED. Sensitivity study of front suspension parameters in elastokinematics and handling behavior of a vehicle. SAE Technical Paper; 2016. Report no.:.
- [9] Shibahata Y, Shimada K, Tomari T. Improvement of vehicle maneuverability by direct yaw moment control. *Vehicle System Dynamics*. 1993;22(5-6):465–481.
- [10] Van Zanten AT. Bosch esp systems: 5 years of experience. SAE Technical Paper; 2000. Report no.:.
- [11] De Novellis L, Sorniotti A, Gruber P. Design and comparison of the handling performance of different electric vehicle layouts. *Proceedings of the Institution of Mechanical Engineers, Part D: Journal of Automobile Engineering*. 2014;228(2):218–232.
- [12] Esmailzadeh E, Goodarzi A, Vossoughi G. Optimal yaw moment control law for improved vehicle handling. *Mechatronics*. 2003;13(7):659–675.
- [13] De Novellis L, Sorniotti A, Gruber P, Orus J, Fortun JMR, Theunissen J, De Smet J. Direct yaw moment control actuated through electric drivetrains and friction brakes: Theoretical design and experimental assessment. *Mechatronics*. 2015;26:1–15.
- [14] Lenzo B, Sorniotti A, Gruber P, Sannen K. On the experimental analysis of single input single output control of yaw rate and sideslip angle. *International Journal of Automotive Technology*. 2017;18(5):799–811.
- [15] Wang Z, Montanaro U, Fallah S, Sorniotti A, Lenzo B. A gain scheduled robust linear quadratic regulator for vehicle direct yaw moment control. *Mechatronics*. 2018;.
- [16] Lenzo B, Sorniotti A, De Filippis G, Gruber P, Sannen K. Understeer characteristics for energy-efficient fully electric vehicles with multiple motors. In: *EVS29 International Battery, Hybrid and Fuel Cell Electric Vehicle Symposium Proceedings*; 2016.
- [17] Farroni F, Lamberti R, Mancinelli N, Timpone F. Trip-id: A tool for a smart and interactive identification of magic formula tyre model parameters from experimental data acquired on track or test rig. *Mechanical Systems and Signal Processing*. 2018;102:1–22.
- [18] De Novellis L, Sorniotti A, Gruber P. Driving modes for designing the cornering response of fully electric vehicles with multiple motors. *Mechanical Systems and Signal Processing*. 2015;64:1–15.
- [19] De Novellis L, Sorniotti A, Gruber P, Pennycott A. Comparison of feedback control techniques for torque-vectoring control of fully electric vehicles. *IEEE Transactions on Vehicular Technology*. 2014;63(8):3612–3623.
- [20] Chindamo D, Lenzo B, Gadola M. On the vehicle sideslip angle estimation: a literature review of methods, models and innovations. *Applied Sciences*. 2018;.
- [21] Frendo F, Greco G, Guiggiani M. Critical review of handling diagram and understeer gradient for vehicles with locked differential. *Vehicle System Dynamics*. 2006;44(06):431–447.
- [22] Frendo F, Greco G, Guiggiani M, Sponzillo A. The handling surface: a new perspective in vehicle

- dynamics. *Vehicle System Dynamics*. 2007;45(11):1001–1016.
- [23] Buchi F, Frendo F. A new formulation of the understeer coefficient to relate yaw torque and vehicle handling. *Vehicle System Dynamics*. 2016;54(6):831–847.
 - [24] Osborn RP, Shim T. Independent control of all-wheel-drive torque distribution. *Vehicle system dynamics*. 2006;44(7):529–546.
 - [25] Edelmann J, Ploch M. Analysis of controllability of automobiles at steady-state cornering considering different drive concepts. *Proceedings of IAVSD 2017 (Dynamics of Vehicles on Roads and Tracks)*. 2018;.
 - [26] Rill G. Reducing the cornering resistance by torque vectoring. *Procedia Engineering*. 2017;199:3284–3289.
 - [27] Buchi F, Lenzo B, Frendo F, De Nijs W, Sorniotti A. The effect of the front-to-rear wheel torque distribution on vehicle handling: an experimental assessment. In: *Dynamics of Vehicles on Roads and Tracks Volume 1: Proceedings of the 25th International Symposium on Dynamics of Vehicles on Roads and Tracks (IAVSD 2017)*, 14-18 August 2017, Rockhampton, Queensland, Australia. CRC Press; 2017. p. 31.
 - [28] Pacejka H. *Tire and vehicle dynamics*. Elsevier; 2005.
 - [29] Genta G. *Motor vehicle dynamics: modeling and simulation*. Vol. 43. World Scientific; 1997.
 - [30] Guiggiani M. *The science of vehicle dynamics: handling, braking, and ride of road and race cars*. Springer Science & Business Media; 2014.
 - [31] Moors E. On the reciprocal of the general algebraic matrix. *Bulletin of the American Mathematical Society*. 1920;9(26):394–95.
 - [32] Ben-Israel A, Greville TN. *Generalized inverses: theory and applications*. Vol. 15. Springer Science & Business Media; 2003.